nature communications

Article

https://doi.org/10.1038/s41467-025-67413-0

Wireless battery-free ultrathin lithium-niobate resonator as wearable and implantable electronics for continuous monitoring of mechanical vital signs

Received: 6 May 2025

Accepted: 30 November 2025

Published online: 12 December 2025

Check for updates

A list of authors and their affiliations appears at the end of the paper

Continuous monitoring of physiological parameters associated with dynamic biomechanics, such as intracranial pressure (ICP) and vital signs, is important for clinical diagnosis of brain diseases and timely medical intervention. Current skin-interfaced and implant technologies face challenges in terms of bulky tethers and/or percutaneous wires with high infection risks. Here, we report the wireless, battery-free, and lightweight devices for both wearable and fully implantable applications. The devices incorporate an ultrathin piezoelectric resonator with suspended lithium niobate thin film (LNTF, 3 μm thick), enabling the wireless tracking of mechanophysiological signals by detecting variations in resonance frequency. We experimentally and computationally establish the operational principles of the resonator sensor and assess the device performance as wearables for dynamically monitoring artery pulse and apnea events during respiration. Implantable wireless pressure sensors adapted from this scheme allow for untethered, minimally invasive ICP sensing with a low detection limit of 0.15 mmHg over a wide range up to 240 mmHg. In vivo experiments performed on rat models validate the device capabilities of accurately capturing clinically relevant ICP variations and elevated levels of ICP under pathophysiological conditions of hydrocephalus, with excellent biocompatibility after long-term implantation periods. These findings create the clinical significance of such battery-less and wireless devices for precise characterization of dynamic biomechanics of living tissues.

Precise and continuous monitoring of physiological signals associated with the dynamic biomechanics of patients provides essential information for establishing clinical diagnostics with in-time treatment protocols and assessing post-surgical recovery. Of particular interest is the advanced bio-integrated system that can enable real-time measurements of tissue biomechanical properties, and continuous track of subtle but clinically meaningful variations under various pathophysiologic conditions. Associated embodiment includes the characterization of vital signs, such as internal organ pressure, respiration rate, and arterial pulse, all of which are of key importance for patients with cerebral pathologies, cardiovascular diseases, hypertension, and compartment syndromes[1–5]. The clinical standards for such purposes typically demand percutaneous catheters for connecting electronic components with external hardware that can induce other complications, including infection and hemorrhage[6,7]. Although useful in many scenarios, these approaches also require multiple connected wires and rigid platforms with large-area metal electrodes, thus inevitably constraining patient mobility and limiting their applications within

e-mail: sem@fudan.edu.cn

hospital settings[8,9]. For example, 23–52% of clinical cases with transcranial catheters have been reported to be infected with meningitis[10,11]. These and other limitations motivate the development of miniaturized, flexible implants that operate wirelessly in battery-free mode, to support conformal contact at biotic/abiotic interfaces and to offer untethered and minimally invasive monitoring of variable mechanophysiological parameters.

Due to the portable designs and mechanical compliance, emerging classes of human-machine-integrated electronics for physiological assessments can establish intimate, functional interfaces with targeted soft tissue for characterizing the biomechanics through different sensing mechanisms, including piezoresistive[12], capacitive[13], triboelectric[14], and piezoelectric[15] methods. State-of-the-art technologies include silicon-nanomembrane (Si-NM) based piezoresistive sensors, with merits of high strain gauge factor, compatibility with MEMS processes, and self-degradation capability. Examples range from conformal sheets for high-precision myocardial infarction locating[16], to three-dimensional strain gauges for vascular pressure sensing[17], and to fully implantable cavity sensors for ICP monitoring[18,19]. Characterization for wireless measurements of these systems relies on active Bluetooth low energy (BLE) or near-field communication (NFC) that typically involves rigid modules, which compromises the overall mechanical compliance and requires reliable post-enclosures for long-term bio-safety within implanted biological tissues[20].

Alternative approaches based on inductor-capacitor (LC) circuits enable the design of implantable devices with simple structure, battery-free, and passive interrogation schemes for wireless measurements of artery pulse[21], intracranial temperature[22], and pressures[23,24] based on the resonance frequency shift. These LC resonator sensors typically incorporate capacitor components with dielectric membranes embedded by parallel electrodes, yielding capacitance change for sensing applications with quality factor (Q) constrained within 3–90 that limits the measurement sensitivity and resolution[21–23,25]. Meanwhile, the trade-off between the sensitivity and the sensing range in the pressure-responsive capacitors leads to limited applications particularly at high pressure levels as reported[24,26,27]. Additionally, ultrasound methods for tracking biomechanical parameters of biotissue rely on handheld single-element piezoelectric transducer with bulky and rigid structure or wearable phased array transducer with complex wire connections[28,29]. When applied in scenarios where bone tissue is present along the propagation path of ultrasonic wave, such as intracranial monitoring, ultrasound devices face the problem of significant signal attenuation and scattering due to acoustic impedance mismatch between bone and soft tissue[30,31]. In many cases, however, these methods either support mechanical sensing that is tailored only for a specific region of the body for a single-functionality use or require complex external electronics for data processing. Therefore, persistent challenges remain in the development of bio-electronic systems with wireless measurement capabilities that can monitor multiple types of dynamic mechanophysiological signals in a fully-implantable, battery-free form.

In this article, we present a tether-free, ultraflexible, and lightweight device for multifunctional monitoring of physiological parameters that supports wireless, continuous measurement of ICP, breathing, and arterial pulse. The sensing component utilizes a transferred ultrathin crystalline LNTF (3 μm thick) with interdigital electrode (IDE) on the surface as a piezoelectric resonator that can provide a remarkably higher quality factor (Q ~ 300) than those of LC resonators. Distinguished to ultrasound technology, such platforms enabled by inductive coupling can support wireless and battery-less tracking of time-dependent mechanophysiological signals in a fully implantable/wearable form. Furthermore, compared to other techniques such as piezoresistive sensors of strain gauges, our devices eliminate the need of Bluetooth energy (BLE) and/or near-field communication (NFC) that typically involves rigid electronic wireless modules. Dynamic mechanophysiological signals at the interface between the device and targeted bio-tissues can induce changes in the IDE period, leading to variation in the frequency of the LNTF resonator that can be measured by an external reader antenna. Simulations and comparative measurements reveal that the suspended structural design of the LNTF significantly enhances the electro-mechanical coupling efficiency of the piezoelectric resonator, and thus the wireless communication performance. Examples of wearable evaluations range from precisely capturing pulse rate and pulse waveform change to real-time detecting apnea events in respiration monitoring. Integration of the LNTF resonator sensor with the air cavity can yield the fully implantable device that enables continuous ICP monitoring with high sensitivity (detection limit of 0.15 mmHg) and minimal invasiveness. The utilization of soft materials, ultrathin design, and miniaturized structure of the wireless device provides the merits of stable operation after implantation for long-term ICP monitoring (28 days). Extensive ex vivo and in vivo assessments confirm the excellent biocompatibility of the device as medical implants, with broad potential for use in clinical medicine and at-home diagnostics.

Results

Materials, integration schemes, and structural design of LNTF-resonator-based wireless device

The battery-free, resonator-based devices form the basis for implantable and wearable capabilities in wireless biomechanical monitoring of physiological signals such as ICP, breathing, and arterial pulse (Fig. 1a), in a continuous, real-time mode of operation. Figure 1b shows the schematic illustration of the system, consisting of (1) an external reader antenna for wireless measurement, (2) a coupling antenna for signal transmission, connected to (3) the ultrathin, flexible bio-integrated sensor that incorporates monocrystalline lithium niobate (LN) membrane and IDE, as the high-frequency piezoelectric resonator for the characterization of biomechanics. The wireless operation of the platform involves the combination of the piezoelectric resonator for sensing and the inductive coupling between the two antennas for signal readout. For the piezoelectric resonator as illustrated in the inset of Fig. 1b, the period length λ of IDE determines its resonance frequency f_0, while the mechanical deformation at the biotic/abiotic interface can yield the period length change (Δλ), thereby resulting in a variation of the resonance frequency (Δf). Such an operational principle can allow the miniaturized design of reader antenna (within 2 cm diameter) to capture the continuous variation of resonance frequency of the underlying resonator in response to applied strain, in a wireless, highly sensitive way. The ultrathin structure and chipless design of the sensor can yield conformal contact via lamination onto different biological targets, thus providing capabilities for both implantable (e.g., brain) and wearable (e.g., skin) measurements of biomechanics, as shown in Fig. 1c.

Figure 1d presents the multilayer materials stack of the implantable/wearable sensor platform, comprising key components of a metal coil (Au, 500 nm thick) as the coupling antenna, an LNTF (3 μm thick) as the resonator, and the interconnected IDE (Au, 200 nm thick), all of which are embedded in polyimide (PI) layers. The fabrication begins with the definition of ultrathin monocrystalline LNTFs on a wafer substrate (lithium niobate on insulator, LNOI), each with dimensions of 1 mm × 1.3 mm, followed by transfer printing the LNTF onto flexible PI interlayers (Supplementary Figs. 1–2). A sequence of assembly steps includes metal deposition, lithographic patterning, and etching to create the IDE array (interval spacing of 15 μm) and the antenna coil (outer diameter of ~1.1 cm), respectively. Here, the top and bottom PI layers serving as encapsulation and substrate can provide stable mechanics that enable efficient delivery of mechanical coupling towards the piezoelectric resonator. Detailed information on fabrication processes appears in the "Methods" section and Supplementary Figs. 3–7. The fabricated device features an ultrathin thickness of ~10 μm and a lightweight of ~3 mg, resulting in excellent mechanical

https://doi.org/10.1038/s41467-025-67413-0

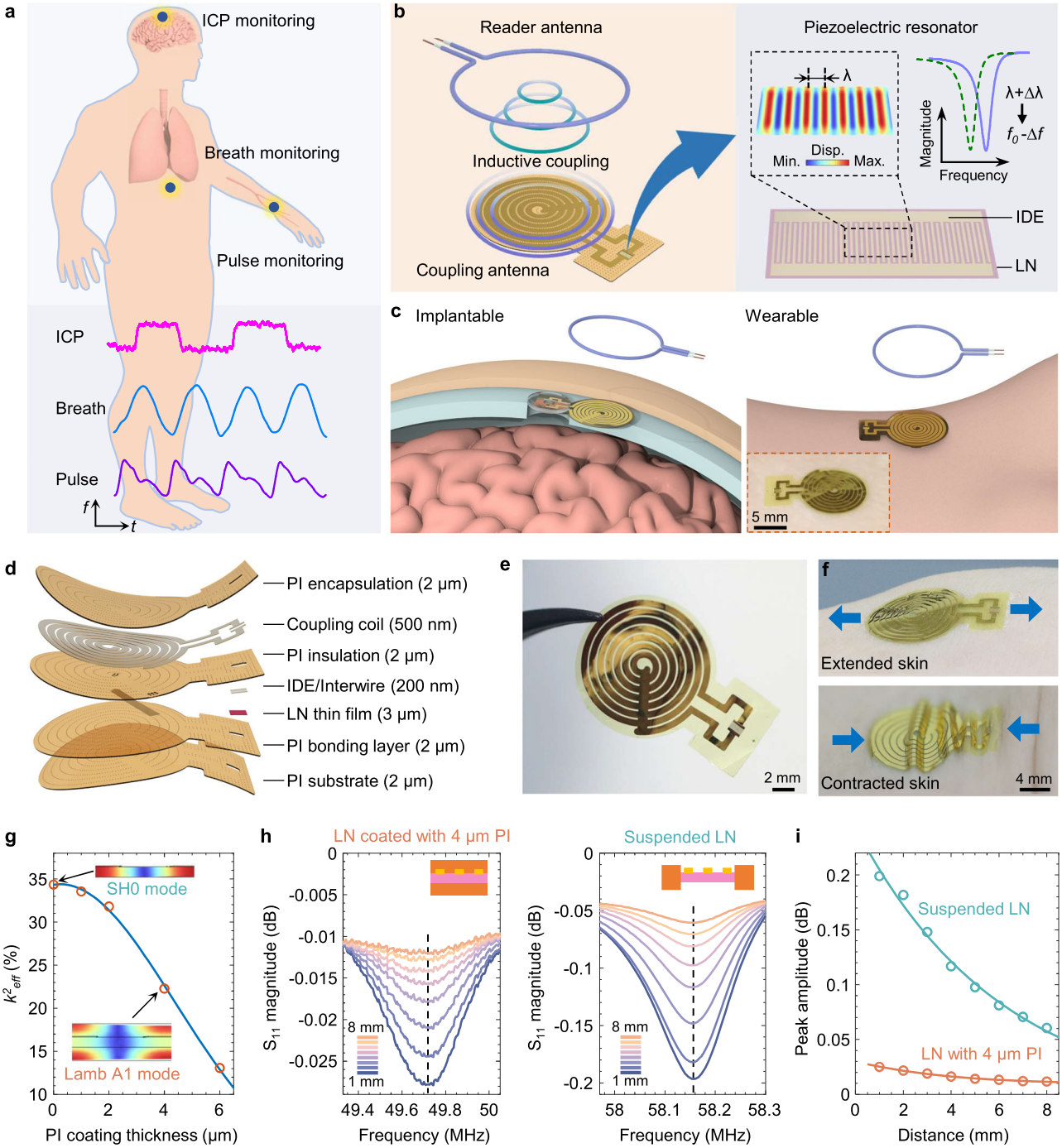

Fig. 1 | Working principle, materials, and design of ultrathin piezoelectric resonator based wireless device. a Schematic illustration of multifunctional physiological signal monitoring of ICP, breath, and artery pulse with the wireless device. **b** Diagram showing the wireless operation mechanism of the device based on the inductive coupling between reader antenna and coupling antenna (left) and the electromechanical coupling of a piezoelectric LN resonator (right). Deformation induced change in the IDE period λ alters the resonance frequency f_0 of the piezoelectric resonator. **c** Illustration of the device implanted in the brain (left) for implantable application and attached to the skin (right) for wearable application, showcasing its wireless, battery-free, flexible, and chipless operation. **d** Exploded-view schematic showing the multilayer structure and materials of the wireless resonator device. **e** Image of the fabricated ultrathin wireless device. **f** Images of the wireless device conformally adhered to stretched skin (top) and compressed skin (bottom), showing the excellent flexibility of the device. **g** Calculated electromechanical coupling efficiency of LNTF resonator as a function of PI coating thickness. Insets show the corresponding resonance mode. **h** Measured reflection spectra of the LNTF resonator with 4 μm thick PI coating and the suspended LNTF resonator at varying reader antenna-device distance. **i** Measured resonance amplitude of LNTF resonators as a function of communication distance.

compliance of the sensor device for intimate contact with soft and curved bio-tissue surfaces under highly dynamic conditions (Fig. 1e, f).

Careful optimization of the materials structure and device design of the piezoelectric resonator with high electromechanical coupling efficiency, guided by computational modeling, can allow for wireless measurements with enhanced signal strength and extended communication distance (Fig. 1g–i). Specifically, Fig. 1g shows the finite element analysis (FEA) results of the effective electromechanical coupling

coefficient k_{eff}^2 of the LNTF resonator (3 μm thick) with IDE configuration defined in Supplementary Fig. 8, as a function of PI coating layer thickness. Increasing the PI thickness shifts the oscillation displacement to the PI layers with a resonance mode transition of the multilayer structure from shear horizontal (SH) to Lamb A1 mode (Supplementary Fig. 9), thus yielding dramatically decreased k_{eff}^2. Benefitted from the significant piezoelectric effect of LN, the results demonstrate that the k_{eff}^2 is up to 35 % for the resonator without any coatings, with the resonance confined in the suspended LNTF structure by SH0 mode. Such a k_{eff}^2 is comparable to those of the SH mode LN resonators (24.8%-40%) fabricated on rigid substrates as previously reported[32,33]. Figure 1h exhibits the experimental reflection spectra of the resonator with 4-μm-thick PI coating and the suspended resonator without PI coating, respectively, at variable distances between the reader antenna and the device (from 1 mm to 8 mm). As summarized in Fig. 1i, the peak amplitudes of measured signals of the suspended LNTF resonator, extracted from Fig. 1h, surpass that of the PI-coated resonator by orders of magnitude, thereby indicating enhanced quality of signal transmission by higher electromechanical coupling effect, which is consistent with the FEA results.

Operational principles of wireless, battery-free measurements

For dynamically sensing in a wireless, high-precision fashion, we fabricated the suspended LNTF-based resonator with high electromechanical coupling efficiency. To achieve the suspended structure of LNTF, Fig. 2a displays scanning-electron-microscope (SEM) images of the LNTF at an ultrathin thickness of 3 μm, before and after transfer printed on flexible PI substrates, respectively. Subsequent etching of the PI layers within specific regions on dual sides of the LNTF can form the suspended resonator, as illustrated in Fig. 2b and Supplementary Fig. 10. Here, the width and pitch of the electrode fingers are designed as 15 μm, yielding an IDE wavelength of 60 μm. Figure 2c shows the optical images of suspended LNTF together with IDE arrays from both front and back views, where the etched PI window with an area of 0.55 mm × 1.1 mm exposes 18 electrode pairs.

For the experimental and theoretical analysis of the suspended-LNTF-based resonator, the use of ringing-down method can collect and record the oscillation signals following RF pulse excitation at different frequencies (Supplementary Note 1 and Supplementary Fig. 11). The result in Fig. 2d plots the oscillation signal of the suspended-LNTF resonator wirelessly excited near its resonance frequency. Exponential fitting of the magnitude envelope by $A(t)=A_0 e^{-t/\tau}$ gives the decay time τ (1.6 μs) when the magnitude drops by a factor of e. Figure 2e shows the spectra of the LNTF resonator, both calculated using FFT algorithm and fitted by the Lorentz function, indicating an eigenfrequency f_0 at 58.163 MHz. For resonator-based sensors, a high quality factor Q is essential for high sensitivity measurement. The Q value of the suspended LNTF resonator in this study can be quantified as ~300 by $Q = \pi f_0 \tau$. Consistently, experimental measurements (Fig. 2f) of the magnitude and phase of the scattering parameter S_{11} using a vector network analyzer (VNA) yield a resonance frequency of 58.163 MHz, in good agreement with that determined by the ringing-down method and the simulation results (Supplementary Fig. 9). It is worth noting that although the configuration of IDE in series with coil inductor of our device can form an LC resonator, introducing an extra resonance peak in the sensor system that well separated with the LNTF resonator (Supplementary Note 2 and Supplementary Fig. 12), the use of the piezoelectric LNTF resonator as the sensing component can provide much better sensitivity and resolution due to the remarkably high quality factor than that of the LC resonator (Q ~ 8.9). In addition, S_{11} measurements of the separate LNTF resonator and the LNTF resonator connected in series with coil inductor in Supplementary Fig. 13 confirm the negligible influence of the inductor on the quality factor of the LNTF resonator. The results in Supplementary Fig. 14 evaluate the wireless transmission between the reader antenna and the wireless LNTF resonator at various relative positions that involve varying vertical, lateral, and rotational alignments of the reader antenna. As expected, the amplitude of the resonance peak decreases monotonically as the misalignment increases, primarily due to the signal attenuation during wireless communication. However, the measured resonance frequency remains stable with Δf fixed at zero in most cases of measurements. Results of Supplementary Fig. 15 show the frequency stability across measurement time at different conditions, with the resonator placed at different distances to the reader antenna (Supplementary Fig. 15a) and upon application on the forearm skin of volunteer human subject (Supplementary Fig. 15b), respectively.

These findings establish the LNTF-based resonator platform for time-dependent measurements of the frequency variation with stable performance for dynamically characterizing variations of biomechanics, such as ICP, cardiac pulse or breathing, by robust wireless power and data transmission. Figure 2g displays the optical images of the LNTF-based resonator mounted on artificial skins of a 2-mm thick poly(-dimethylsiloxane) (PDMS) layer (elastic modulus $E = 500$ kPa) under different deformation conditions of stretching and bending, with stretching elongation within 5% and bending radius of 2 cm, respectively. Insets of Fig. 2g show the strain distribution within the device obtained by FEA simulations, indicating maximum internal principal strains of 0.29%, 0.85%, and 3.49% in the LNTF, the gold wire, and the PI layer. These values are well below the corresponding fracture strain of LN (> 0.35%), gold film (~6%), and PI materials (~10%)[34–36], respectively. Detailed results of FEA simulations under various physical conditions appear in Supplementary Fig. 16, all of which indicate excellent flexibility and mechanical robustness of the bio-integrated platforms.

In this context, Fig. 2h and Supplementary Fig. 17 present the results of wireless strain measurements (experimental setup appears in Supplementary Fig. 18) under periodic deformation of the artificial skin (2 mm thick PDMS substrate) along the IDE direction, at different strain intensities ranging from 0.03 to 4%. Specifically, the strain sensing principle of the LNTF resonator relies on the frequency shift induced by the IDE period change when the piezoelectric film is subjected to deformation. Theoretically, Δf and the eigenfrequency of the resonator, f_0, satisfy the following function, $\Delta f = -f_0 \cdot \varepsilon/(1+\varepsilon)$, where ε stands for the strain of the LNTF along the IDE direction. Supplementary Fig. 19 shows the simulation results of the strain within the LNTF as a function of stretching strain (0-6%) applied onto the PDMS substrate. Consistently, Fig. 2i plots the experimental Δf as a function of LNTF strain, revealing an intrinsic sensitivity of 56.9 Hz•με^{-1} as the slope of the results, which is consistent with the theoretical value (f_0, fundamental frequency of the resonator), as well as in agreement with previously reported studies[37,38]. Meanwhile, investigation on the resonant frequency change of the LNTF resonator and the entire sensor system in response to separately applied strain on different parts of the device (LNTF part and the coil inductor part) in Supplementary Fig. 20 confirms the independence of the LNTF frequency on the inductance change of the coil inductor under deformation. Additional characterization by periodic tensile cycles validates the capability of the wireless device for time-dependent measurements at different period durations (Supplementary Fig. 21). In long-term cyclic strain tests at various strain intensities (Supplementary Fig. 22 and Fig. 2j), the continuous monitoring up to 5000 cycles remains stable without any notable performance degradation and baseline drift. As a consequence, these results indicate the feasibility of such LNTF-based resonators for potential use in high-precision mechanophysiological measurements, thus proving the stability and durability with a minimum detectable strain of lower than 0.03%.

Wearable application in real-time monitoring mechanophysiological signals of arterial pulse and respiration

A key advantage of our flexible device compared to sensors that contain rigid electronic components is that it can form a conformal

https://doi.org/10.1038/s41467-025-67413-0

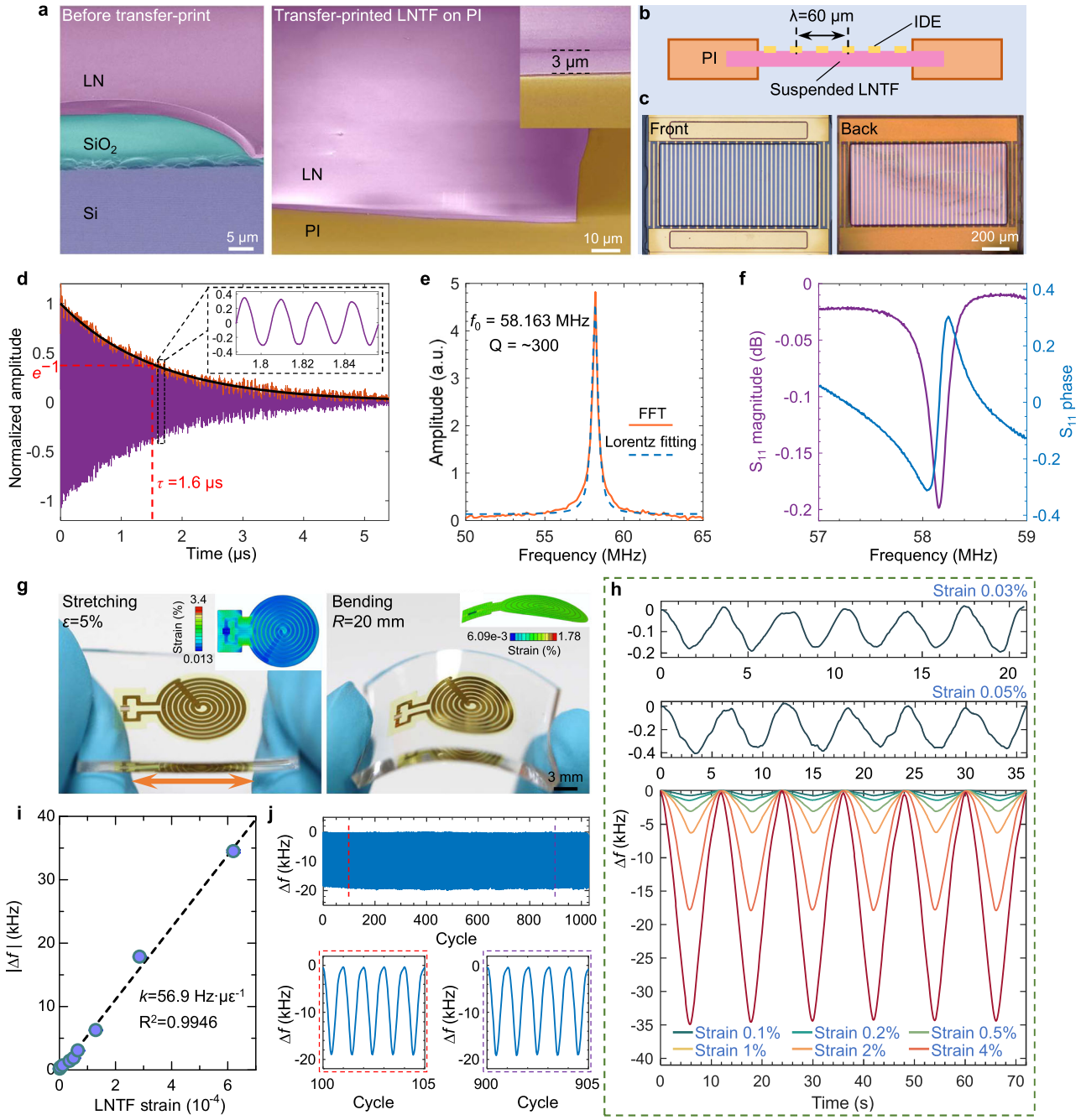

Fig. 2 | Performance characterization of the suspended LNTF based wireless resonator device. a SEM images of the 3 μm thick monocrystalline LNTF before (left) and after (right) been transfer-printed from LNOI onto a PI substrate. Representative images of five independent measurements are shown. **b** Schematic illustration showing the cross-section structure of the suspended LNTF resonator with the IDE wavelength λ = 60 μm. **c** Optical images of the suspended LN film and the IDE on LN surface in finally fabricated device. The etched PI window exposes an area of 0.55 × 1.1 mm² with 18 pairs of electrodes on the resonator center. **d** Oscillation signal of the suspended LNTF resonator device wirelessly measured using the ringing-down method. The inset shows a magnified view of the oscillation signal. Solid black line indicates the exponential fitting by $A(t)=A_0 \cdot e^{-t/\tau}$ with the constant A_0 and the decay time τ. **e** FFT-calculated and fitted resonance spectra of the LNTF resonator. **f** Measured reflection coefficient of the wireless device. **g** Photograph of the flexible device attached to a PDMS substrate under stretching (left) and bending (right) deformation. The inset shows FEA simulation results of the maximum principal strain distribution in the device. **h** Resonance frequency shift of the wireless resonator sensor under PDMS substrate strain of different magnitudes. **i** Linear relationship between the frequency shift of the wireless sensor and the strain imposed on the LN film. **j** Frequency response of the wireless sensor to long-term periodic stretching load at PDMS substrate strain of 2% over 1000 cycles.

contact interface with target biological tissues, as illustrated in Fig. 3a, that serve as wearable wireless electronics for human subjects. As an example, Fig. 3b presents the mechanism of pulse monitoring with the wireless LNTF-based resonator sensor, where the arterial pulses generate dynamic, subtle strain of the related bio-tissues (i.e., blood vessels, skin, *etc.*) and thus induce variation of resonance frequency that can be measured in a wireless, battery-free manner. Figure 3c shows representative examples of pulse waveforms from a human individual measured by the LNTF-based resonator sensor (purple lines), well resembling the simultaneously recorded signal by photoplethysmography (PPG) method (green lines, Pulse Sensor, Your Cee Co. Ltd). For the PPG sensors, the measurement sites typically locate in

https://doi.org/10.1038/s41467-025-67413-0

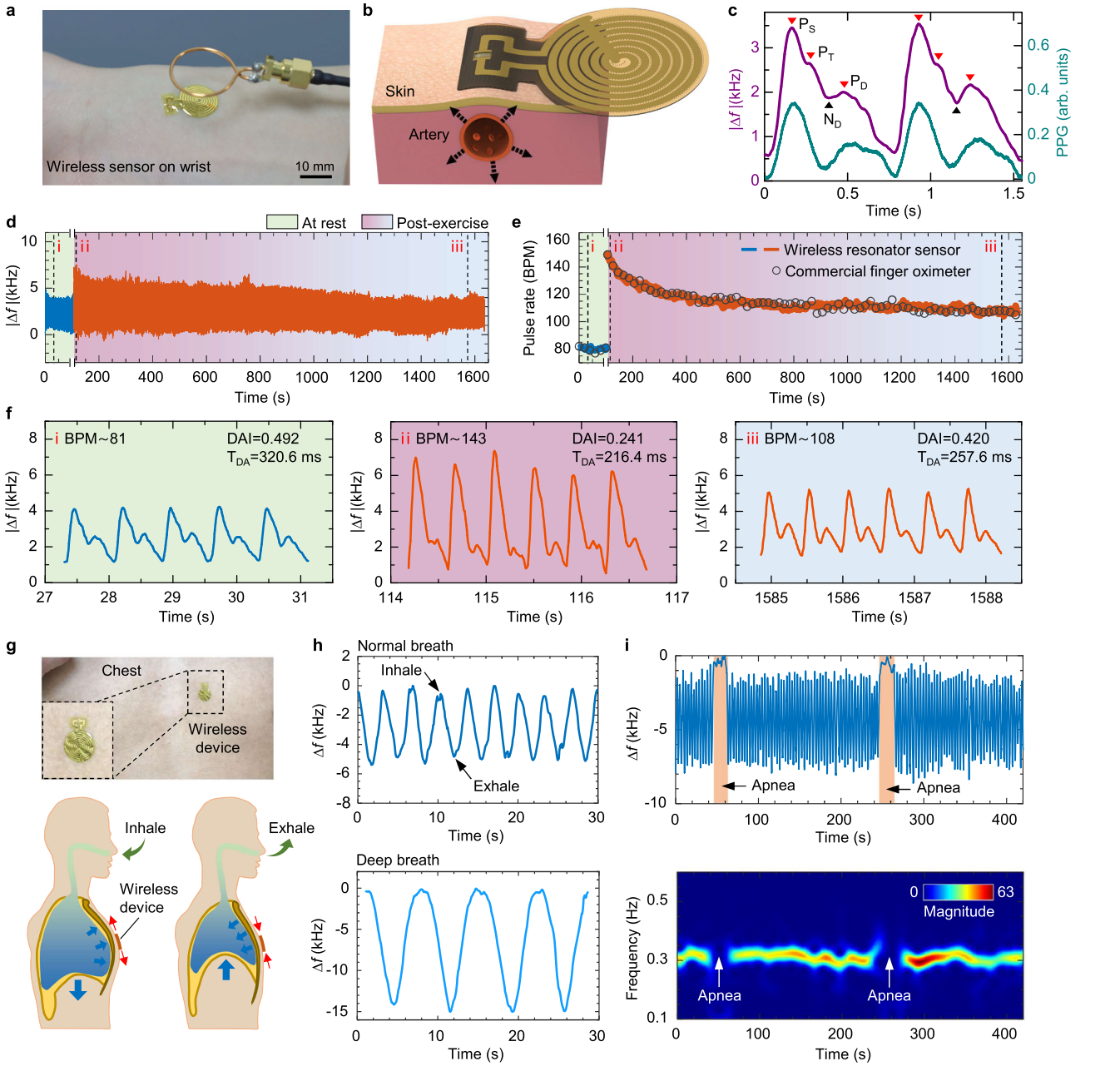

Fig. 3 | Wearable application of the LNTF-resonator-based strain sensor in wireless monitoring of physiological signals. a Photograph of the wireless strain sensor adhering to the wrist skin seamlessly for radial artery pulse monitoring. **b** Schematic showing the mechanism of pulse detection with the LNTF-resonator-based sensor. **c** Representative arterial pulse waveforms recorded by the wireless sensor and the PPG method, showing the feature points of systolic peak (P_S), tidal peak (P_T), dicrotic notch (N_D), and diastolic peak (P_D). **d** Continuous monitoring of pulse waveform during rest and after exercise. Dashed lines indicate different time points including (i) resting, (ii) directly after exercise, and (iii) 25 min post-exercise. **e** Comparison of the pulse rate change over time, as recorded by the wireless strain sensor and a commercial oximeter, showing consistent trends. **f** Enlarged pulse waveforms at different stages with calculated diastolic augmentation index (DAI) and time of diastolic augmentation (T_{DA}). **g** (top) Photograph of the wireless strain sensor laminated on the chest for breath monitoring. (bottom) Schematic showing the mechanism of respiration monitoring by detection of skin strain caused by the changes in thoracic volume. **h** Detected respiratory signals during normal breath (top) and deep (bottom) breath cycles. **i** Recorded respiration signal with apnea events (top) and time-frequency analysis of the corresponding respiration signal (bottom).

the microvascular system on the skin surface, such as the earlobe and fingertip, because of the insufficient penetration depth of light into tissue[39]. The challenge lies in the accurate recording of pulse waveforms with detailed characteristics due to signal acquisition from the capillaries rather than the arterial sites, with consideration of the susceptibility of PPG sensors to ambient light and skin curvature, as reported in previous studies[40,41]. As a comparison, the waveforms obtained by our piezoelectric resonator device with high quality factor exhibit distinguishable feature points compared to those by PPG method, including the distinct systolic peak (P_S), tidal peak (P_T), dicrotic notch (N_D), and diastolic peak (P_D)[42,43].

In addition, clinical PPG devices commonly involve rigid components (such as battery) and require constant pressure on the skin to ensure stable device-skin contact for good signal quality, which can cause discomfort to the subjects during prolonged use[44]. By contrast, the excellent skin conformability and light weight (~3 mg) features of

our ultrathin device provide the comfortable wearability with a stable device-skin interface for on-demand measurements without disturbing patients' daily life. As a demonstration, arterial pulse monitoring with the wireless device laminated on the wrist artery site via a thin layer of PDMS adhesion gel (base: curing agent = 40:1) was performed during a consecutive wearing of 12 h on each day, over a period of one week (Supplementary Fig. 23). The results indicate consistent functionality without signal degradation or skin irritation during the entire monitoring period.

The values of these peaks can provide informative clinical results of importance, such as radial diastolic augmentation index (DAI_r) and interval time of diastolic augmentation (T_{DA}) between P_D and P_S, defined as $DAI_r = P_D/P_S$ and $T_{DA} = T_{PD} - T_{PS}$, respectively. For example, the results of Supplementary Fig. 24 yield measurements of DAI_r and T_{DA} as 0.50 and 319.2 ms of a volunteer subject (30 years old, male) under rest conditions, respectively, consistent with those of human individuals (ages under 35, e.g., DAI_r = 0.2–0.6 and T_{DA} = 200-50 ms) as reported in the previous literatures[12,45,46]. Such parameters can offer clinical significance for monitoring human health conditions, such as evaluation of cardiovascular function, where disorders of vascular sclerosis typically involve decrease in artery elasticity and thus an increase of DAI_r and decrease of T_{DA}[47,48].

Furthermore, characterizing the change of mechanophysiological signals under conditions associated with human kinesiology is of particular interest. Here, Fig. 3d and Supplementary Fig. 24b compare the measurement results of continuous monitoring of pulse waveforms of human subjects during different states, such as rest, at-exercise (rapid walking), and post-strenuous exercise, respectively. As expected, the results under post-exercise conditions (orange data) reveal gradually weakening amplitudes from Δf of ~6 kHz down to the level of 3 kHz over time, indicating decreased blood pressure after exercise within 30-min continuous measurements. Correspondingly, Fig. 3e shows the real-time monitoring of pulse rate (in beats per minute, bpm) captured by the LNTF-based resonator sensor (solid data) at the conditions of rest and post-exercise, both well consistent with the measurements using a commercial finger oximeter (hollow data, OMRON HPO-100). Here, the results display the similar trend, where the pulse rate increases from the rest state of 81 bpm to 140 bpm right after exercise, and subsequently decreases with time, approaching 108 bpm that comparable to the level of the at-rest condition over measurements. Further analysis of the pulse waveforms recorded at different timescale stages appears in Fig. 3f, including (i) resting, (ii) directly after exercise, and (iii) 25-min post-exercise, corresponding to results of DAI_r as 0.49, 0.24, and 0.42, and of T_{DA} as 320.6 ms, 216.4 ms, and 257.6 ms, respectively. In all of these cases, the LNTF-based resonator sensor can precisely track the variation of pulse waveforms associated with various cardiovascular conditions, establishing the potential use as wearable, wireless systems.

Alternative wearable application involves continuous monitoring of breathing. Figure 3g exhibits an optical image of the LNTF-based resonator mounted on the chest skin of a human subject (30-year-old, male). For the real-time tracking of the respiration, inhaling and exhaling of air into the lung can yield subtle variations of thoracic volume, thus resulting in time-dependent strain across the surface of the chest skin, as illustrated in the bottom of Fig. 3g. In this manner, Fig. 3h collects two groups of real-time tracking data, including respiration under normal conditions (upper) and deep-breath conditions (bottom), respectively. Specifically, inhale- and exhale-process cycles can lead to increase and decrease of applied strain at the device/skin interfaces, which correspond to the peak and valley of the tracked frequency shift of Δf. As a comparison, deep breath can yield higher amplitudes of Δf and lower respiration rates compared to those of normal breath, consistent with expectations.

Beyond simply capturing repeatable respiration, the LNTF-based resonator sensor can also provide diagnosis of abnormal respiration related to specific pathophysiologic conditions, such as sleep apnea syndrome (SAS), which refers to a breathing disease of clinical significance[49,50]. In this context, continuous tracking of the respiration of the patient during sleep states is important, particularly in a wireless, wearable measurement format. Figure 3i provides the tracking of Δf upon device application onto the chest surface of human subjects, for dynamic assessment of SAS that can be simulated by involving respiration apnea at specific time points. As an illustration, the time-frequency analysis of measured Δf by short-time Fourier transform (STFT) at the bottom of Fig. 3i reveals a frequency component near 0.3 Hz, corresponding to a respiration rate of ~18 cycle·min^{-1}. Specifically, apnea events that occur at ~50 seconds and at ~250 seconds can be captured as notable interruptions in the frequency component line, in good agreement with the continuous tracking of Δf. Additional measurements in Supplementary Fig. 25 investigate the effect of motion artefacts on the measurement results during continuous monitoring of respiration with introduced body movements. Although the motions of leaning forward and stretching can cause signal fluctuation and shift, the frequency response recovers to normal baseline level after the movements (Supplementary Fig. 25a). In addition, time-frequency domain analysis of the signal by STFT can extract the target information (respiration rate as indicated by the black dashed line) with stable measurements even in the presence of external interference (Supplementary Fig. 25b). These findings suggest the potential of the resonator device for dynamically characterizing physiological information in clinical health diagnosis.

Fully implantable, wireless modules for ICP monitoring

Precise and continuous measurement of internal pressures within organ systems provides essential biological information for both diagnosis and treatment guidance of various diseases[51–55]. Of particular interest is ICP monitoring for patients with cerebral pathologies, such as traumatic brain injury (TBI), hydrocephalus, and ischemic stroke[56–58]. However, clinically available wired devices that fulfill this function require percutaneous leads for power supply and signal transmission, which increase infection risk and restrict patient mobility[59,60]. In order to avoid the percutaneous catheter, fully implantable and wireless ICP monitors for long-term continuous application have been developed, such as the AURA™ ICP monitoring system, the M.scio® sensor reservoir, and the Neurovent® P-tel system that have been approved by the Food and Drug Administration (FDA)[61–63]. These outlined sensor implants, however, typically involve disc-shaped housings encapsulated by rigid materials (titanium, Peek, and ceramics) with relatively large overall thickness (4.3–7.6 mm)[64], which can cause complications including localized ischemia and disordered wound healing of overlying scalp after implantation. As a comparison, Fig. 4a shows the schematic illustration of the LNTF resonator device mounted on the skull, serving as a fully implantable pressure sensor that enables wireless, minimally invasive monitoring of ICP in a battery-free, real-time operation mode. Here, the implantable platform incorporates the wireless resonator sensor integrated on a thin PDMS substrate by the SiO_2 bonding layer (100 nm thick), designed with an air cavity in the center (width: 2 mm, length: 2.2 mm, depth: 400 μm) for pressure sensing (Fig. 4b). Detailed fabrication processing appears in "Methods" section and Supplementary Fig. 26. As shown in the cross-sectional schematic in the Supplementary Fig. 27, the resultant device architecture forms the suspended LNTF-based resonator to seal the air cavity that enables the measurements of various external pressures.

The FEA results in Fig. 4c reveal the dependence of the vertical displacement of the suspended LNTF and the corresponding strain distribution on applied pressure that is comparable to the magnitudes of ICP (here, we take 30 mmHg as an example). Specifically, the increase of the applied pressure can lead to variation of electrode spacing along the IDE array direction, and thus yield the resonance

https://doi.org/10.1038/s41467-025-67413-0

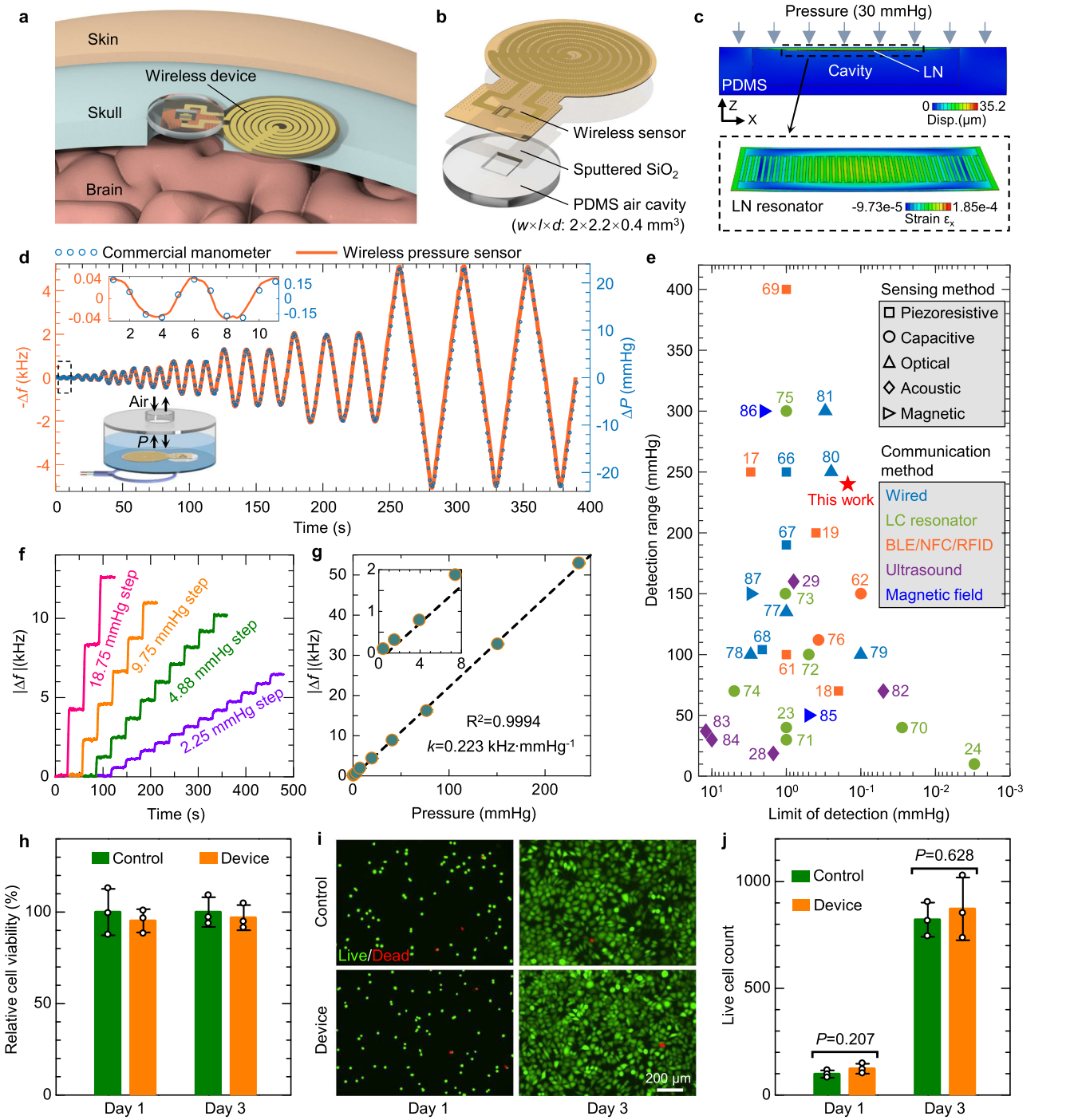

Fig. 4 | Wireless pressure sensor with the LNTF resonator. a Schematic of the implanted wireless device mounted on the skull for ICP sensing. **b** Schematic illustration of the wireless pressure sensor, showing the LNTF resonator device, sputtered SiO_2 layer (thickness of 100 nm), and the PDMS substrate (5 mm in diameter, 0.6 mm in thickness) with an air cavity ($w \times l \times d$: $2 \times 2.2 \times 0.4$ mm^3). **c** FEA simulation of the LNTF deformation and strain distribution under an applied pressure of 30 mmHg. **d** Frequency shifts of the wireless pressure sensor under various applied pressures ranging from 0.15 mmHg to 23 mmHg. **e** Performance comparison between proposed wireless pressure sensor and reported devices for implantable application. Pressure sensing method is indicated by marker shapes while communication methods for signal transmission are categorized by different colors. **f** Frequency shift in response to different incremental pressure steps. **g** Calibration curve of frequency shift versus pressure. **h** Quantitative viability of L929 cells in control group and device group after incubation period of 1 and 3 days. Data are means ± S.D., $n = 3$ independent samples. **i** Fluorescence images of cells cultured with the device on day 1 and day 3. Green (calcein AM) and red color (propidium iodide) indicate live and dead cells, respectively. **j** Comparison of the viable cell count derived from the live/dead staining assay. Data are means ± S.D., $n = 3$ independent samples. Statistical analysis was performed by unpaired two-tailed Student's t test, where $p < 0.05$ represents significant difference.

frequency shift, output through the wireless sensor antenna. Notably, results of FEA modeling (Supplementary Fig. 28) indicate that increasing the applied pressure (from 3 mmHg to 200 mmHg) can significantly enhance the resulting strain within the suspended LNTF resonator by orders of magnitude. To evaluate the wireless communication capability of the device under fully implanted conditions, Supplementary Fig. 29 shows the application of such a device underneath the porcine skin at various thicknesses (1–12 mm) with the reader

antenna attached on top to record the signal, suggesting excellent communication stability between the resonator sensor and the reader antenna.

In this context, the suspended structure of LNTF resonator sensor and the air cavity, together with the outside reader system, can characterize the mechanical properties of a range of biological targets both in vitro and in vivo. As illustrated in the schematic diagram of Fig. 4d, in vitro measurements that mimic pressure conditions inside intracranial space can assess the ICP monitoring capability of the device at various physical states. Here, an airtight chamber connected to a syringe and a commercial manometer as comparison allows real-time pressure adjustment inside the chamber (details appear in Supplementary Fig. 30). Results of continuous monitoring of the inside pressure, both using the LNTF-based resonator sensor (Δf, orange lines) and commercial manometer (ΔP, blue dots), are well consistent in Fig. 4d, yielding a pressure-sensing resolution as high as 0.15 mmHg (upper inset). Further characterization with various pressure levels (up to 240 mmHg), as shown in Supplementary Figs. 31–33, suggests stable capabilities of the device for measurements of pressure covering the typical range in ICP monitoring (0-100 mmHg) under different pathophysiologic conditions[65].

Highly sensitive ICP recording is important both for monitoring of severe ICP elevation and for the extraction of useful information from subtle ICP fluctuations; therefore, continuing efforts have been devoted to developing ICP sensors that can provide a low detection limit over a wide range. Figure 4e summarizes the performance of various devices for biomedical pressure sensing with key parameters of measurement range and detection limit, as reported from previous literature, including piezoresistive[17–19,61,66–69], capacitive[23,24,62,70–76], optical[77–81], acoustic[28,29,82–84], and magnetic methods[85–87]. Specifically, the piezoresistive pressure sensors can offer a wide detection range (typically from 100 mmHg to 400 mmHg), but their wireless sensing usually requires rigid components such as BLE, NFC, or RFID modules. Capacitive pressure sensors integrated with LC circuit resonators that enable wireless applications typically have low quality factors and present a trade-off between detection limit and range[26]. Examples include an ultrasensitive ICP device that utilizes an iontronic capacitor operating at the exceptional point (EP) with a detection of 0.003 mmHg for pressures within 0-10 mmHg[24] and wireless LC pressure sensors for monitoring of ICP up to 150 mmHg with a detection limit of 1 mmHg[73]. Optical pressure sensors can provide both wide detection range and low sensing limit. However, wireless measurements are challenging to realize due to the inevitable use of optic fibers. Clinical ultrasound methods for noninvasive ICP measurement, including the transcranial Doppler ultrasonography (TCD) and optic nerve sheath diameter (ONSD) assessment, fail to provide sufficiently accurate results for continuous monitoring in routine practice[88]. For transcranial ultrasound monitoring of ICP with implanted devices, replacement of a part of skull bone with acoustically transparent materials is required to enhance ultrasonic penetration[82]. Other appealing wireless implants based on magnetic field typically work in an active manner with complex sensing modules, including separate excitation and receiver units, as well as amplifiers for detection of weak magnetic signal. By comparison, our LNTF-based wireless resonator sensor with high quality factor provides a high sensitivity with a detection limit of 0.15 mmHg. Meanwhile, the measurement range of 240 mmHg satisfies the minimum range requirement of 100 mmHg for ICP devices, as specified in the standards developed by the Association for the Advancement of Medical Instrumentation (AAMI)[89].

In addition, Fig. 4f shows the frequency monitoring of the LNTF-based resonator sensor in real-time response to stepwise pressure loading cycles, indicating stable plateaus during each holding step without any notable creep effect. Specifically, the plot of Δf against applied pressure provides a linear relationship with high sensitivity at a slope of 0.223 kHz·mmHg^{-1}, as extracted in Fig. 4g. Further evaluations of frequency response at various repeated pressure amplitudes appear in Supplementary Fig. 34, where the long-term tests demonstrate the operational stability and robustness of the device over 1000 cycles.

To validate the feasibility of employing our wireless LNTF resonator device for in vivo application, we evaluated device biocompatibility with cytotoxicity assessment (Fig. 4h–j). Figure 4h presents the comparative results of the co-culturation of L929 rat fibroblast cells with the sensor after 1 and 3 days in CCK-8 assay, indicating a negligible difference in quantitative cell viability compared to the control group. Figure 4i demonstrates the fluorescent images of live/dead cell staining of the device group and the control group on day 1 and day 3, both of which illustrate similar cell morphology and proliferation rates between the two groups (Fig. 4j). Details can be found in "Methods" section. These results indicate that the LNTF-based resonator sensors are nontoxic and biocompatible to biological tissues, suggesting the potential use as wireless implants for stable operation.

In vivo monitoring of ICP on a living rat model

In vivo, real-time ICP measurement in a rat model demonstrates the clinical applicability of our LNTF resonator-based pressure sensor. Figure 5a showcases the schematic illustration of in vivo ICP monitoring of living rats, with the implants of the ultrathin, flexible LNTF resonator sensor and the wearables of the top reader antenna. Here, the implantation procedures involve craniotomy surgery by drilling a window through the skull (diameter of 5 mm), followed by integrating the device across the cranial opening and sealing with light-curable dental cement, as illustrated in Fig. 5b. Such methods can anchor the device and thereby connect the resonator sensor to the intracranial space, for dynamically and minimally-invasive monitoring in vivo ICP (Fig. 5c). In parallel, applications of commercial pressure sensor on the opposite side of skull opening can simultaneously track ICP, as comparative results to those of LNTF-based resonator sensor (Supplementary Fig. 35). Details of the animal tests appear in "Methods" section. We analyzed the impact of various noise sources and measurement parameters on the baseline stability of recorded frequency and the pressure sensing performance of the wireless ICP sensor in terms of result deviation and time resolution (Supplementary Note 3 and Supplementary Fig. 36). The measurement system enables a frequency output rate of 10 S·s^{-1} with a low noise-induced fluctuation of ±0.016 kHz (corresponding to a pressure deviation of ±0.07 mmHg) that can support real-time, high-sensitivity ICP monitoring for this study. Moreover, Supplementary Fig. 37 shows frequency response of the wireless ICP sensor to pressure change measured at different reader-device distances (from 2 mm to 8 mm). Although the noise-induced frequency fluctuation tends to increase with increasing distance, the detection limit of 0.15 mmHg can still be achieved at a distance of 8 mm, confirming the robustness of our device for wireless operation in practical applications.

Here, the technologies of micro-computed tomography (Micro-CT) can be used for visualizing the implants in vivo, because of their wide availability, non-invasiveness, and fast modes of image acquisition. Figure 5d and Supplementary Fig. 38 show the Micro-CT images of the wireless resonator sensor implanted into the head of a living rat 5 days post-surgery, with a set of images including device implantation position (upper in Fig. 5e) and craniotomy defect (bottom in Fig. 5e). Details can be found in "Methods" section. For the measurement setup, Fig. 5f shows the photograph of the in vivo ICP monitoring, with the resonator sensor completely implanted into the rat brain and the top reader antenna for data recording. Acute ICP variations are introduced by periodically squeezing the rat flank. Such abdominal compression can cause an increase of intra-abdominal pressure of the rat, and thus, in turn, increases the ICP[90,91]. Consequently, Fig. 5g records the real-time ICP of the living rat based on the implanted resonator sensor (orange lines) in response to different levels of squeeze in cycles, in good agreement with those measured by commercial tools (blue dots)

https://doi.org/10.1038/s41467-025-67413-0

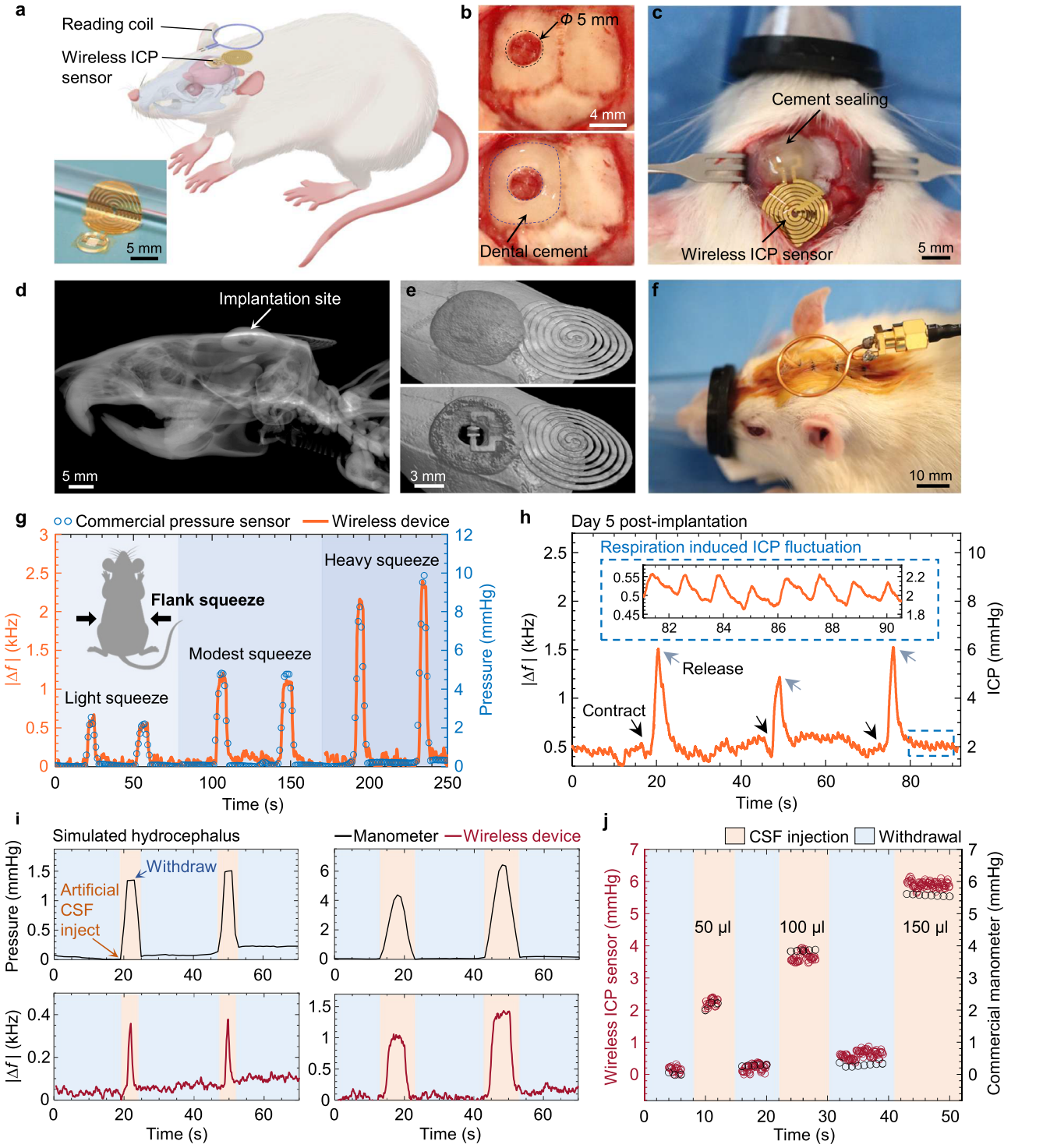

Fig. 5 | In vivo wireless ICP sensing in a rat model. a Diagram of the wireless sensor implanted in the brain of a rat model for wireless ICP sensing. Inset shows the photograph of the flexible wireless pressure sensor conformally wrapped around a cylindrical rod. **b** The craniotomy preparation including a 5 mm-diameter cranial window for implantation. **c** Photograph of the wireless ICP sensor mounted on a rat skull. Dental cement bonds to the skull around PDMS substrate and seals the craniotomy opening. **d** Micro-CT image of the sensor implanted in the brain of a living rat on day 5 following implantation. **e** Top view micro-CT images showing the location of the implant (top) and the craniotomy defect beneath the ICP sensor (bottom). **f** Photograph showing in vivo ICP measurement of a rat implanted with the wireless device. **g** In vivo recording of variations in ICP due to contracting and releasing the rat flank with different compression intensities. **h** Frequency changes of the wireless ICP sensor and corresponding ICP variation induced by abdomen compression of the rat on day 5 post-implantation. The inset shows respiration-induced ICP baseline fluctuation. **i** Monitoring of ICP changes in simulated hydrocephalus by injection of artificial CSF. **j** Comparison between ICP changes recorded by the wireless ICP sensor and commercial pressure sensor in response to CSF volume change.

that span a range of 10 mmHg. As consistent with previous reports[85], the enhancement of the squeeze extent can increase the magnitudes of ICP in vivo, examples of which show an increase from 2.5 mmHg (light) to 10 mmHg (heavy) in our cases. By comparison, Fig. 5h presents the results of ICP monitoring of a rat after 5 days following implantation. The modest squeeze yields an increase of ICP by ~4 mmHg, which is consistent with the results of the acute test in Fig. 5g. Due to the low detection limit of our device, the subtle ICP variation induced by intrathoracic pressure change with respiration can be recorded as periodic shifts in the frequency baseline[65], where the time-frequency domain analysis (Supplementary Fig. 39) indicates a respiration rate near 0.8 Hz of the anesthetized rat. The ICP shift of the rat model caused by respiration is around ~0.2 mmHg in this study, which is comparable with those of other animal models (0.3 mmHg in rabbit)[24].

In addition, the use of implantable, wireless ICP monitors can offer powerful capabilities for diagnostic utility of various brain diseases and neurological disorders. As an example, we performed the continuous ICP measurements for monitoring of hydrocephalus in terms of various related pathological conditions (Fig. 5i). Here, the injection of different volumes of artificial cerebrospinal fluid (CSF) into the rat brain can yield varying elevated ICPs to simulate the extent of hydrocephalus[82,92]. Specifically, injection of CSF increases the ICP, and withdrawal of CSF leads to a decrease in ICP, respectively. As illustrated in Fig. 5i, the continuous monitoring via ICP sensor provides the recorded $|\Delta f|$ (red) that well resembles those measured by commercial manometer (black). As a comparison, Fig. 5j summarizes the measurement results of ICP acquired by the resonator sensor (red) depending on the changes of CSF volumes (50, 100, 150 μL), with good consistency with those obtained by the manometer.

To investigate the performance stability of our wireless ICP device for long-term use, we conducted experiments for both in vitro and in vivo applications. The sensor response to applied pressure collected on different day by immersing the device in PBS solution at the body temperature (37 °C) indicate consistent pressure response and a stable sensitivity of ~0.2 kHz/mmHg over a period of four weeks as shown in Supplementary Fig. 40. For in vivo evaluation (Supplementary Fig. 41) with a living rat model, the ICP measurements recorded on Day 1, Day 14, and Day 28, in terms of frequency response of implanted device upon acute ICP changes by abdomen compression of the rat confirm accurate ICP monitoring with stable performance across weeks to months. Supplementary Table 1 compares key features of existing ICP sensors, highlighting the advantages of our device in regard to superior sensing performance, miniaturized size, and long-term functionality for implanted applications.

Further assessment of in vivo biocompatibility over an extended timescale confirms the biosafety of the wireless ICP sensor as brain implants. Results in Supplementary Fig. 42 demonstrate the soaking test for determination of content species of released elements (i.e., Li, Nb, Cr, Au) within biofluids, during different timescales of immersion of the resonator sensor (from 1 week to 5 weeks) in PBS solution (200 mL, pH 7.4, 37 °C). Here, the inductively coupled plasma-mass spectrometry (ICP-MS) results indicate increases in the concentration of these elements upon immersion duration, all of which are well below the toxicity levels in adults according to previous reports[93,94]. Immuno-fluorescence images in Supplementary Fig. 43 show the brain tissues from the rat implanted with devices for two months that are stained by DAPI, GFAP, and CD68 for recognizing the cell nuclei, astrocytes, and macrophages, respectively. These images suggest the absence of abnormal inflammation activity compared with that of the control rat without implants. Additionally, histological analysis by haematoxylin and eosin (H&E) staining of the major organs (brain, heart, liver, spleen, lung, and kidney) obtained from a rat implanted with the device for two months and a control rat reveals no sign of systematic inflammation or organ damage (Supplementary Fig. 44). These results together validate the biological feasibility of the ICP sensors for the use of fully-implantable, wireless platforms.

Discussion

The results presented here demonstrate ultrathin devices that integrate an LNTF resonator with a coupling antenna for continuous, wireless sensing of subtle physiological signals induced by physiological activities. The distinguishing features compared with reported wireless devices utilizing rigid BLE or NFC modules are the flexible and chipless design, which allows for conformal attachment to the tissue, thereby alleviating the mechanical property mismatch and improving mechanical coupling at the device-tissue interface. Wearable applications as demonstrated in the monitoring of vital signs with high levels of accuracy and reliability, suggest the potential of the device to complement existing clinical-standard systems. Furthermore, the wireless and battery-free feature eliminates the need for percutaneous wires and periodic replacement of power sources, making it particularly advantageous in implanted scenarios. In vivo experiments performed on rat models by mounting the LNTF resonator-based pressure sensor on the skull highlight the capability of continuous ICP monitoring in a wireless and minimally invasive manner. Cytotoxicity assessment and analysis of released element content, along with the immunofluorescent and histological studies on the brain and other main organs of the rats implanted with the device for extended periods reveal the absence of toxic effects or immune reactions. Taken together, the wireless communication scheme, miniaturized size, flexible form factor, and excellent biocompatibility may form the basis for future biomedical electronics capable of measuring physiological signals and disease-related internal pressures.

Future work will focus on integrating multichannel piezoelectric resonators through the frequency-multiplexed method, which can maintain the miniaturized size of the device while providing simultaneous and multifunctional sensing of different parameters. In addition, further optimization of the electrical impedance matching between the piezoelectric resonator and the coil inductor will be carried out for enhanced power transmission efficiency, and thus higher signal strength and communication range. Another future opportunity lies in the utilization of alternative biodegradable materials to construct wireless resonator devices that enable programmed bioresorbable properties after a predesigned operation period for simplifying surgical procedures and extending the range of clinical applications.

Methods

Fabrication of the free-standing LNTF

Fabrication began with mechanical back-grinding of the LNOI wafer (128Y-cut LN ~ 3 μm, buried SiO_2 ~ 2 μm, Si substrate ~500 μm; NANOLN) to reduce the Si substrate thickness (200 μm). Dicing the wafer yielded LNOI blocks with in-plane dimensions of 1 mm × 1.3 mm. Immersing the blocks in tetramethyl ammonium hydroxide (TMAH, 10%; Adamas) for 8 h at 90 °C fully removed the silicon substrate. Subsequent buried oxide etching in hydrogen fluoride solution (HF, 42%) for 5 min, followed by sufficient rinsing with deionized water, yielded the free-standing LNTF (thickness ~3 μm).

Fabrication of the wireless LNTF resonator device

Preparation of the glass substrate for device fabrication involved spin-casting polymethyl methacrylate (PMMA, 950 A7, ~1 μm; MicroChem) and PI (thickness ~2 μm; Ya'an New Material) on a glass slide, as the sacrificial layer and the supporting layer, respectively. Baking the glass substrate at 230 °C for 2 h fully cured the PI layer. Spin-casting a second PI layer (thickness ~2 μm), followed by partial curing at 110 °C for 20 s formed the bonding layer. Transfer-printing of the LNTF involved picking up the LNTF with a PDMS stamp (base:curing agent = 4:1, Sylgard 184; Dow Corning) and pressing the stamp onto the PI bonding layer. Deposition of Cr/Au (5 nm/200 nm) by magnetron sputtering

(PVD-400; SKY Technology) and wet etching through photolithographically (MA6; SUSS) patterned photoresist mask (S1813, 1.5 μm; Dow) defined the IDE and the interwire. Another PI coating (thickness ~2 μm) served as the isolation layer. Selective removal of PI by oxygen-reactive ion etching (RIE, T2; Trion) with patterned mask (AZ4620, ~10 μm; MicroChemicals) opened the VIAs. Magnetron sputtering deposited a second layer of Cr/Au (10 nm/500 nm), followed by photolithography and wet etching to define the coupling coil (11 mm in diameter) with a track width of 0.75 mm and a trace width of 0.6 mm. Spin coating another PI layer encapsulated the device. Patterned RIE of PI defined the window for exposing the LNTF and created the perfusion hole array (diameter of 50 μm) for dissolving the underlying PMMA layer. PMMA removal by immersing the device in acetone released the device from the glass substrate. Laminating the device, with the IDE side facing down, onto another PMMA-coated glass slide, followed by RIE of the PI window on the other side of LNTF finished the fabrication process.

Assembly of the wireless pressure sensor

Pouring the PDMS mixtures (base:curing agent = 4:1) into a PMMA mould and curing at 70 °C for 10 h produced the PDMS substrates (600 μm in thickness, 5 mm in diameter) with an air cavity (dimensions of $2 \times 2.2 \times 0.4\ mm^3$). Sputtered SiO_2 (100 nm) onto the PI encapsulation of the resonator device with a PDMS block covering the resonator region served as the bonding layer. Oxygen plasma treatment (300 mTorr, 45 s; PDC-32G, Harrick Plasma) of the PDMS substrate and the device activated the surfaces for bonding. Careful alignment of the PDMS substrate with the wireless device located the LNTF in the center of the air cavity. Following bonding enhancement performed on a hot plate at 80 °C for 20 min finished the assembly of the wireless pressure sensor.

FEA simulation of electromechanical coupling coefficient

Simulations of the suspended LNTF resonator and the resonator coated by PI layers were performed using COMSOL Multiphysics 6.1 through the solid mechanics and the electrostatics interfaces. The resonators were modeled in 3D geometry with the 3 μm thick 128Y-cut LN, the IDE (Au 200 nm), and the PI layers of different thicknesses on both sides of the LN. The top and bottom boundaries of the resonator were set as free boundary conditions. Mechanical loss was included in the models through an isotropic loss factor of 0.002. Eigenfrequency study was first carried out to investigate the resonance mode and obtain the eigenfrequency. In the following frequency-domain analysis, a unit voltage and ground were applied to the electrode ports. The admittance of the resonator was then calculated as a function of selected frequency range. The effective electromechanical coupling coefficient of the LNTF resonator is calculated according to[95]:

$$K_{eff}^2 = \frac{\pi^2(f_p^2 - f_s^2)}{8f_s^2} \quad (1)$$

where the f_s and f_p are the resonance and anti-resonance frequencies extracted from the admittance curve.

Real-time recording of resonance frequency

For real-time recording of the resonance frequency of the resonator device, a customized interface programmed with LabVIEW 2021 (National Instruments) enabled the control of the VNA (ZNL 6, Rohde & Schwarz) and signal processing. Connecting a reader coil (diameter of 2 cm) to one port of the VNA allowed wireless measurement of the scattering parameter S_{11} (power of 0 dBm) of the device. Lorentz function fitting to the magnitude data of S_{11} determined the resonance frequency. Here, the software interface supports the control of frequency ranges, frequency points, and sweep average number for S_{11} measurements, as well as the spectrum fitting for resonance frequency determination, enabling the automatic output of frequency response in real time at a maximum rate of 100 $S{\cdot}s^{-1}$.

Wearable applications in pulse and breath monitoring

For wearable application of the wireless device in pulse and breath monitoring, the device was transferred on water-soluble tape and laminated onto the wrist or the chest for measuring artery pulse or respiration, with a layer of bio-glue (Derma-tac, Smooth-On Inc.) serving as the adhesives. The water-soluble tape was then dissolved and completely removed with DI water. For repeated detachment and lamination, application of sticky PDMS gel (base:curing agent = 40:1) as an alternative adhesion layer enabled multiple uses of the device.

In vitro pressure sensing test

The in vitro pressure measurement involved placing the wireless pressure sensor inside an airtight chamber partially filled with PBS solution. Connecting a syringe pump (PHD ULTRA, Harvard Apparatus) with the chamber and a commercial manometer (510i, Testo) via a tee connector and plastic tubes enabled control of the pressure inside the chamber. Placing a reader coil connected to the VNA near the wireless pressure sensor allowed for measurement of the sensor response to pressure change.

In vivo ICP monitoring

Adult male rats (Sprague-Dawley, weighing 250–350 g, 7–9 weeks) were fully acclimatized for 7 days before surgery. The animals were anesthetized using isoflurane gas (4% for induction and 2% for maintenance) and fixed in a stereotaxic frame during the surgical procedures. The device implantation process involved the head skin sterilization, creation of craniectomy defect (diameter ~5 mm) on the skull, removal of dura mater, fixation of the device on the cortical surface, sealing of the cranial window with dental cement (Transbond XT, 3 M), and suture of the skin. Placing a reader coil above the rat head (distance ~ 1 mm) enabled monitoring of the ICP change upon squeezing and releasing the rat flank. For the hydrocephalus rat model, insertion of a polyurethane tube (inner diameter of 1 mm) on the contralateral side that connected with an injector and a commercial pressure sensor allowed the injection of artificial CSF and provided comparative ICP results. To assess the stability and performance of the wireless sensor with time, ICP measurements were performed on different days after the implantation. Micro-CT (SkyScan 1276, Bruker) images were taken to check the condition of the device inside the rat head.

In vivo biocompatibility assessment

For evaluation of inflammation response, the brain tissue from rats implanted with the device for two months and from control rats were immunostained for glial fibrillary acidic protein (GFAP) to detect astrocytes and CD68 to identify microglia/macrophages. Briefly, the dissected brains were post-fixed in 4% paraformaldehyde solution, dehydrated with gradient ethanol, embedded in paraffin wax, followed by sample sectioning (RM2016, Leica). The prepared section slides were then blocked in 3% bovine serum albumin (BSA) for 50 min and incubated with the primary antibodies (mouse anti-GFAP, 1:500, Servicebio, GB113109; rabbit anti-CD68, 1:200, Servicebio, GB15096) overnight at 4 °C. After washing three times with PBS, the sections were then incubated with the secondary fluorescent antibodies of goat anti-mouse IgG (CY3 conjugated, 1:300, Servicebio, GB21301) and goat anti-rabbit IgG (Alexa Fluor 488 conjugated, 1:400, Servicebio, GB25303) for 50 min, followed by nuclei staining with 4′,6-diamidino-2-phenylindole (DAPI) for 10 min. In addition, H&E staining was performed on the organ slides from the brain and other main organs, including heart, liver, spleen, lung, and kidney. Section images were finally obtained using a digital slide scanner (Pannoramic MIDI, 3DHISTECH).

Ethics

All human tests involved simple device contact without physical modification of the skin or invasive measurement. The experiments were conducted by protocols approved by the Ethics Committee of Tongji Hospital Affiliated to Tongji University (approval no. 2025-173). Informed consent was obtained from all participants before inclusion in this study. All animal experiments were performed in accordance with the guidelines of the Institutional Animal Care and Use Committee and approved by the Animal Committee of Laboratory Animal Center at Fudan University (approval no. 202312020S) and by the Shengchang Biotechnology Co. Ltd. (approval no. 2024-08-FDDX-SEM-114).

Reporting summary

Further information on research design is available in the Nature Portfolio Reporting Summary linked to this article.

Data availability

All data supporting the findings of this study are available within the article and its supplementary files. Any additional requests for information can be directed to, and will be fulfilled by, the corresponding authors. Source data are provided with this paper.

References

1. Dunn, L. T. Raised intracranial pressure. *J. Neurol. Neurosurg. Psychiatry* **73**, i23–i27 (2002).
2. Brogan, M. E. & Manno, E. M. Treatment of malignant brain edema and increased intracranial pressure after stroke. *Curr. Treat. Options Neurol.* **17**, 327 (2014).
3. Yacoub, M. H. & McLeod, C. The expanding role of implantable devices to monitor heart failure and pulmonary hypertension. *Nat. Rev. Cardiol.* **15**, 770–779 (2018).
4. Huang, Q. F. et al. Ambulatory blood pressure monitoring to diagnose and manage hypertension. *Hypertension* **77**, 254–264 (2021).
5. Malbrain, M. L. N. G. et al. Results from the international conference of experts on intra-abdominal hypertension and abdominal compartment syndrome. I. Definitions. *Intensive Care Med.* **32**, 1722–1732 (2006).
6. Braun, M. U. et al. Percutaneous lead implantation connected to an external device in stimulation-dependent patients with systemic infection—a prospective and controlled study. *Pacing Clin. Electrophysiol.* **29**, 875–879 (2006).
7. Tetens, M. M. et al. Use of intensive care, intracranial pressure monitoring, and external ventricular drainage devises in patients with bacterial meningitis, a cohort study. *Acta Neurochir.* **166**, 287 (2024).
8. Bonner, O., Beardsall, K., Crilly, N. & Lasenby, J. There were more wires than him': the potential for wireless patient monitoring in neonatal intensive care. *BMJ Innov.* **3**, 12–18 (2017).
9. Koydemir, H. C. & Ozcan, A. Wearable and implantable sensors for biomedical applications. *Annu. Rev. Anal. Chem.* **11**, 127–146 (2018).
10. Hetem, D. J., Woerdeman, P. A., Bonten, M. J. M. & Ekkelenkamp, M. B. Relationship between bacterial colonization of external cerebrospinal fluid drains and secondary meningitis: a retrospective analysis of an 8-year period. *J. Neurosurg.* **113**, 1309–1313 (2010).
11. Dorresteijn, K. R. I. S., Jellema, K., van de Beek, D. & Brouwer, M. C. Factors and measures predicting external CSF drain-associated ventriculitis. *Neurology* **93**, 964–972 (2019).
12. Li, S. et al. Monitoring blood pressure and cardiac function without positioning via a deep learning–assisted strain sensor array. *Sci. Adv.* **9**, eadh0615 (2023).
13. Song, J. et al. Polyelectrolyte-based wireless and drift-free iontronic sensors for orthodontic sensing. *Sci. Adv.* **11**, eadu6086 (2025).
14. Pu, X., An, S., Tang, Q., Guo, H. & Hu, C. Wearable triboelectric sensors for biomedical monitoring and human-machine interface. *iScience* **24**, 102027 (2021).
15. Li, J. et al. Thin, soft, wearable system for continuous wireless monitoring of artery blood pressure. *Nat. Commun.* **14**, 5009 (2023).
16. Hu, B. et al. Ultrathin crystalline silicon–based omnidirectional strain gauges for implantable/wearable characterization of soft tissue biomechanics. *Sci. Adv.* **10**, eadp8804 (2024).
17. Kwon, K. et al. A battery-less wireless implant for the continuous monitoring of vascular pressure, flow rate and temperature. *Nat. Biomed. Eng.* **7**, 1215–1228 (2023).
18. Kang, S. K. et al. Bioresorbable silicon electronic sensors for the brain. *Nature* **530**, 71–76 (2016).
19. Shin, J. et al. Bioresorbable pressure sensors protected with thermally grown silicon dioxide for the monitoring of chronic diseases and healing processes. *Nat. Biomed. Eng.* **3**, 37–46 (2019).
20. Feiner, R. & Dvir, T. Tissue–electronics interfaces: From implantable devices to engineered tissues. *Nat. Rev. Mater.* **3**, 17076 (2017).
21. Boutry, C. M. et al. Biodegradable and flexible arterial-pulse sensor for the wireless monitoring of blood flow. *Nat. Biomed. Eng.* **3**, 47–57 (2019).
22. Lu, D. et al. Bioresorbable, wireless, passive sensors as temporary implants for monitoring regional body temperature. *Adv. Healthc. Mater.* **9**, 2000942 (2020).
23. Lin, J. et al. Wireless bioelectronics for in vivo pressure monitoring with mechanically-compliant hydrogel biointerfaces. *Adv. Mater.* **36**, 2400181 (2024).
24. Li, J. et al. An ultrasensitive multimodal intracranial pressure biotelemetric system enabled by exceptional point and iontronics. *Nat. Commun.* **15**, 9557 (2024).
25. Huang, Q. A., Dong, L. & Wang, L. F. LC passive wireless sensors toward a wireless sensing platform: status, prospects, and challenges. *J. Microelectromech. Syst.* **25**, 822–841 (2016).
26. Ha, K. H., Huh, H., Li, Z. & Lu, N. Soft capacitive pressure sensors: trends, challenges, and perspectives. *ACS Nano* **16**, 3442–3448 (2022).
27. Yuan, H. et al. Progress and challenges in flexible capacitive pressure sensors: Microstructure designs and applications. *Chem. Eng. J.* **485**, 149926 (2024).
28. Wang, M., Jia, L., Jia, X., Li, H. & Feng, X. Flexible circuit-free system via passive modulated ultrasound for wireless thoracic pressure monitoring. *Sci. Adv.* **11**, eads5634 (2025).
29. Wang, C. et al. Monitoring of the central blood pressure waveform via a conformal ultrasonic device. *Nat. Biomed. Eng.* **2**, 687–695 (2018).
30. Ren, J., Li, J., Chen, S., Liu, Y. & Ta, D. Unveiling the potential of ultrasound in brain imaging: Innovations, challenges, and prospects. *Ultrasonics* **145**, 107465 (2025).
31. Rabut, C. et al. Functional ultrasound imaging of human brain activity through an acoustically transparent cranial window. *Sci. Transl. Med.* **16**, eadj3143 (2024).
32. Faizan, M. & Villanueva, L. G. Frequency-scalable fabrication process flow for lithium niobate based Lamb wave resonators. *J. Micromech. Microeng.* **30**, 015008 (2020).
33. Wu, S. et al. High-performance SH-SAW resonator using optimized 30° YX-LiNbO3/SiO2/Si. *Appl. Phys. Lett.* **120**, 242201 (2022).
34. Xu, H. et al. Flexible surface acoustic wave strain sensor based on single crystalline $LiNbO_3$ thin film. *Appl. Phys. Lett.* **112**, 093502 (2018).
35. Luo, X. M. & Zhang, G. P. Deformation-mechanism dependent stretchability of nanocrystalline gold films on flexible substrates. *J. Mater. Res.* **32**, 3516–3523 (2017).

36. Cheng, Y. K., Campéon, B. D. L., Obata, S. & Nishina, Y. Synergic effect of graphene oxide and boron nitride on the mechanical properties of polyimide composite films. *Nanoscale Adv.* **4**, 2339–2345 (2022).
37. He, X. et al. Bendable ZnO thin film surface acoustic wave devices on polyethylene terephthalate substrate. *Appl. Phys. Lett.* **104**, 213504 (2014).
38. Kelly, L., Chen, C., Bao, X. & Berini, P. High-resolution surface acoustic wave (SAW) strain sensor based on acoustic fabry-pérot resonance. *Sens. Actuator A: Phys.* **338**, 113504 (2022).
39. Charlton, P. H. et al. Wearable photoplethysmography for cardiovascular monitoring. *Proc. IEEE* **110**, 355–381 (2022).
40. Zuo, W., Wang, P. & Zhang, D. Comparison of three different types of wrist pulse signals by their physical meanings and diagnosis performance. *IEEE J. Biomed. Health* **20**, 119–127 (2016).
41. El-Hajj, C. & Kyriacou, P. A. Cuffless blood pressure estimation from PPG signals and its derivatives using deep learning models. *Biomed. Signal Process. Control* **70**, 102984 (2021).
42. Chu, Y. et al. Human pulse diagnosis for medical assessments using a wearable piezoelectret sensing system. *Adv. Funct. Mater.* **28**, 1803413 (2018).
43. Liu, T. et al. Multichannel flexible pulse perception array for intelligent disease diagnosis system. *ACS Nano* **17**, 5673–5685 (2023).
44. Scardulla, F. et al. Photoplethysmograhic sensors, potential and limitations: Is it time for regulation? A comprehensive review. *Measurement* **218**, 113150 (2023).
45. Yang, J. C. et al. Microstructured porous pyramid-based ultrahigh sensitive pressure sensor insensitive to strain and temperature. *ACS Appl. Mater. Interfaces* **11**, 19472–19480 (2019).
46. Munir, S. et al. Exercise reduces arterial pressure augmentation through vasodilation of muscular arteries in humans. *Am. J. Physiol. Heart Circ. Physiol.* **294**, H1645–H1650 (2008).
47. Nichols, W. Clinical measurement of arterial stiffness obtained from noninvasive pressure waveforms. *Am. J. Hypertens.* **18**, 3S–10S (2005).
48. Yang, J. et al. Eardrum-inspired active sensors for self-powered cardiovascular system characterization and throat-attached anti-interference voice recognition. *Adv. Mater.* **27**, 1316–1326 (2015).
49. Shen, S. et al. Advances in wearable respiration sensors. *Mater. Today* **72**, 140–162 (2024).
50. Shang, J. et al. A flexible catheter-based sensor array for upper airway soft tissues pressure monitoring. *Nat. Commun.* **16**, 287 (2025).
51. Zhou, S. et al. Clinical validation of a wearable ultrasound sensor of blood pressure. *Nat. Biomed. Eng.* **9**, 865–881 (2025).
52. Cao, Z. et al. A high-stability pressure-sensitive implantable memristor for pulmonary hypertension monitoring. *Adv. Mater.* **37**, 2411659 (2024).
53. Han, M. et al. Catheter-integrated soft multilayer electronic arrays for multiplexed sensing and actuation during cardiac surgery. *Nat. Biomed. Eng.* **4**, 997–1009 (2020).
54. Li, C. et al. Noninvasive, wireless and real-time bladder pressure monitoring with biomimetic structured devices. *Appl. Mater. Today* **29**, 101635 (2022).
55. Kim, J. et al. A soft and transparent contact lens for the wireless quantitative monitoring of intraocular pressure. *Nat. Biomed. Eng.* **5**, 772–782 (2021).
56. Eftekhari, S., Westgate, C. S. J., Johansen, K. P., Bruun, S. R. & Jensen, R. H. Long-term monitoring of intracranial pressure in freely-moving rats; impact of different physiological states. *Fluids Barriers CNS* **17**, 39 (2020).
57. Heldt, T., Zoerle, T., Teichmann, D. & Stocchetti, N. Intracranial pressure and intracranial elastance monitoring in neurocritical care. *Annu. Rev. Biomed. Eng.* **21**, 523–549 (2019).
58. Zoerle, T. et al. Intracranial pressure monitoring in adult patients with traumatic brain injury: challenges and innovations. *Lancet Neurol.* **23**, 938–950 (2024).
59. Uldall, M. et al. A novel method for long-term monitoring of intracranial pressure in rats. *J. Neurosci. Methods* **227**, 1–9 (2014).
60. Zhang, X. et al. Invasive and noninvasive means of measuring intracranial pressure: a review. *Physiol. Meas.* **38**, R143–R182 (2017).
61. Mitchell, K. A. S. et al. First-in-human experience with integration of wireless intracranial pressure monitoring device within a customized cranial implant. *Oper. Neurosurg.* **19**, 341–350 (2020).
62. Antes, S. et al. Intracranial pressure–guided shunt valve adjustments with the Miethke Sensor Reservoir. *World Neurosurg.* **109**, e642–e650 (2018).
63. Velazquez Sanchez, V. F., Al Dayri, G. & Tschan, C. A. Long-term telemetric intracranial pressure monitoring for diagnosis and therapy optimisation of idiopathic intracranial hypertension. *BMC Neurol.* **21**, 343 (2021).
64. Norager, N. H., Lilja-Cyron, A., Hansen, T. S. & Juhler, M. Deciding on appropriate telemetric intracranial pressure monitoring system. *World Neurosurg.* **126**, 564–569 (2019).
65. Abraham, M. & Singhal, V. Intracranial pressure monitoring. *J. Neuroanaesthesiol. Crit. Care.* **2**, 193–203 (2018).
66. Koskinen, L. O. D. & Olivecrona, M. Clinical experience with the intraparenchymal intracranial pressure monitoring Codman Microsensor system. *Neurosurgery* **56**, 693–698 (2005).
67. Allin, D., Czosnyka, M. & Czosnyka, Z. Laboratory testing of the Pressio intracranial pressure monitor. *Neurosurgery* **62**, 1158–1161 (2008).
68. Yang, Q. et al. Materials, mechanics designs, and bioresorbable multisensor platforms for pressure monitoring in the intracranial space. *Adv. Funct. Mater.* **30**, 1910718 (2020).
69. Antes, S., Tschan, C. A., Heckelmann, M., Breuskin, D. & Oertel, J. Telemetric intracranial pressure monitoring with the Raumedic Neurovent P-tel. *World Neurosurg.* **91**, 133–148 (2016).
70. Wang, F. et al. A novel intracranial pressure readout circuit for passive wireless LC sensor. *IEEE Trans. Biomed. Circuits Syst.* **11**, 1123–1132 (2017).
71. Lu, D. et al. Bioresorbable wireless sensors as temporary implants for in vivo measurements of pressure. *Adv. Funct. Mater.* **30**, 2003754 (2020).
72. Chen, L. Y. et al. Continuous wireless pressure monitoring and mapping with ultra-small passive sensors for health monitoring and critical care. *Nat. Commun.* **5**, 5028 (2014).
73. Wei, Q. et al. Optimization of LC sensor enabling wireless passive intracranial pressure monitoring. *Microsyst. Technol.* **25**, 3437–3446 (2019).
74. Behfar, M. H. et al. Inductive passive sensor for intraparenchymal and intraventricular monitoring of intracranial pressure. *Proc. IEEE 38th Annu. Int. Conf. Eng. Med. Biol. Soc.* 1950-1954 (2016).
75. Brugts, J. J. et al. Remote haemodynamic monitoring of pulmonary artery pressures in patients with chronic heart failure (MONITOR-HF): a randomised clinical trial. *Lancet* **401**, 2113–2123 (2023).
76. Cheng, W. et al. Frictionless multiphasic interface for near-ideal aero-elastic pressure sensing. *Nat. Mater.* **22**, 1352–1360 (2023).
77. Piper, I., Barnes, A., Smith, D. & Dunn, L. The Camino intracranial pressure sensor: is it optimal technology? An internal audit with a review of current intracranial pressure monitoring technologies. *Neurosurgery* **49**, 1158–1165 (2001).
78. Shin, J. et al. Bioresorbable optical sensor systems for monitoring of intracranial pressure and temperature. *Sci. Adv.* **5**, eaaw1899 (2019).
79. Zhou, M. D., Yang, C., Liu, Z., Cysyk, J. P. & Zheng, S. Y. An implantable fabry-pérot pressure sensor fabricated on left ventricular assist device for heart failure. *Biomed. Microdevices* **14**, 235–245 (2012).

80. Cottler, P. S., Karpen, W. R., Morrow, D. A. & Kaufman, K. R. Performance characteristics of a new generation pressure microsensor for physiologic applications. *Ann. Biomed. Eng.* **37**, 1638–1645 (2009).
81. Pinet, E., Pham, A. & Rioux, S. Miniature fiber optic pressure sensor for medical applications: an opportunity for intra-aortic balloon pumping (IABP) therapy. *Proc. SPIE* **5855**, 234–237 (2005).
82. Tang, H. et al. Injectable ultrasonic sensor for wireless monitoring of intracranial signals. *Nature* **630**, 84–90 (2024).
83. Ragauskas, A., Daubaris, G., Dziugys, A., Azelis, V. & Gedrimas, V. Innovative non-invasive method for absolute intracranial pressure measurement without calibration. *Acta Neurochir. Suppl.* **95**, 357–361 (2005).
84. Robba, C. et al. Non-invasive intracranial pressure assessment in brain injured patients using ultrasound-based methods. *Acta Neurochir. Suppl.* **126**, 69–73 (2018).
85. Wan, J. et al. Millimeter-scale magnetic implants paired with a fully integrated wearable device for wireless biophysical and biochemical sensing. *Sci. Adv.* **10**, eadm9314 (2024).
86. Gleich, B., Schmale, I., Nielsen, T. & Rahmer, J. Miniature magnetomechanical resonators for wireless tracking and sensing. *Science* **380**, 966–971 (2023).
87. Zulkifli, N. A. B. et al. Highly reliable magnetic-based pressure sensor utilizing simple microstructured PDMS: mechanical and design analysis via finite element analysis. *IEEE Sens. J.* **21**, 16560–16567 (2021).
88. Robba, C. et al. Brain ultrasonography: methodology, basic and advanced principles and clinical applications. A narrative review. *Intensive Care Med.* **45**, 913–927 (2019).
89. Bratton, S. L. et al. VII. Intracranial pressure monitoring technology. *J. Neurotrauma* **24**, S45–S54 (2007).
90. Bloomfield, G. L., Ridings, P. C., Blocher, C. R., Marmarou, A. & Sugerman, H. J. A proposed relationship between increased intra-abdominal, intrathoracic, and intracranial pressure. *Crit. Care Med.* **25**, 496–503 (1997).
91. Deeren, D. H., Dits, H. & Malbrain, M. L. N. G. Correlation between intra-abdominal and intracranial pressure in nontraumatic brain injury. *Intensive Care Med.* **31**, 1577–1581 (2005).
92. Anwar, F. et al. Hydrocephalus: An update on latest progress in pathophysiological and therapeutic research. *Biomed. Pharmacother.* **181**, 117702 (2024).
93. WHO. Trace elements in human nutrition and health. (World Health Organization, Geneva, 1996).
94. Ramos, P., Pinto, E., Santos, A. & Almeida, A. Reference values for trace element levels in the human brain: A systematic review of the literature. *J. Trace Elem. Med. Biol.* **66**, 126745 (2021).
95. Huang, S. et al. $LiNbO_3$ surface acoustic wave resonators with large effective electromechanical coupling. *Electronics* **12**, 2964 (2023).

Acknowledgements

This work was supported by the STI 2030-Major Project: 2022ZD0209900 (E.S.), the National Natural Science Foundation of China: 62204057 (E.S.), 62304044 (L.Z.), 12425204 (F.X.) and 12372096 (F.X.), Science and Technology Commission of Shanghai Municipality: 22ZR1406400 (E.S.), China Postdoctoral Science Foundation: 2023M730712 (L.Z.), Lingang Laboratory: LGL-8998-09 (E.S.), National Key R&D Program of China: 2022YFB3204800 (Z.D.), CAS Project for Young Scientists in Basic Research: YSBR-081 (Z.D.), Strategic Priority Research Program of the Chinese Academy of Sciences: XDB0670000 (Z.D.), Shanghai Municipal Science and Technology Major Project: 2018SHZDZX01 (E.S.), ZJ laboratory, Shanghai Center for Brain Science and Brain-Inspired Technology, and the young scientist project of MOE innovation platform. Part of the device fabrication was conducted in the Fudan Nanofabrication Lab.

Author contributions

L.Z. and E.S. conceived the idea and designed the study. L.Z. and P.L. designed and fabricated the devices. L.Z. designed data acquisition software. L.Z., P.L., W.Y., Z.W. and D. X. performed finite-element analyses. J.Liu and Y.S. assessed biocompatibility. L.Z., P.L., J.Liu, W.Y., Z.W., B.H., Y.L., N.H., J.Li, Z.L., F.L., X.W., L.M. and E.S. performed experiments and analyzed data. M.W., Z.D., R.L., Y.B., F.X., Y.M. and E.S. contributed to experimental investigation and validation. L.Z. and E.S. wrote the manuscript. All authors read and provided comments on the paper.

Competing interests

The authors declare no competing interests.

Additional information

Supplementary information The online version contains supplementary material available at https://doi.org/10.1038/s41467-025-67413-0.

Correspondence and requests for materials should be addressed to Enming Song.

Peer review information *Nature Communications* thanks the anonymous, reviewers for their contribution to the peer review of this work. A peer review file is available.

Lianjie Zhou[1,2,10], Pengchuan Liu[1,2,3,10], Junhan Liu[1,2,3], Wenlou Yuan[4], Zhongyuan Wu[1,2], Dian Xu[5], Bofan Hu[1,2,3], Yuting Shao[6], Yifei Lu[1,2,3], Ningge Huang[1,2,3], Jiahao Li[1,2,3], Zhongzheng Li[1,2,3], Fuying Liang[1,2,3], Xiaojun Wu[1,2,3], Lichao Ma[1,2,3], Ming Wang[7], Zengfeng Di[4], Rui Li[5], Yanlong Bi[6], Fan Xu[8], Yongfeng Mei[1,2,3] & Enming Song[1,2,3,7,9] ✉

[1]Institute of Optoelectronics & College of Future Information Technology, Shanghai Frontiers Science Research Base of Intelligent Optoelectronics and Perception, Department of Materials Science, Fudan University, Shanghai, China. [2]International Institute for Intelligent Nanorobots and Nanosystems, Fudan University, Shanghai, China. [3]Yiwu Research Institute of Fudan University, Yiwu, Zhejiang, China. [4]State Key Laboratory of Materials for Integrated Circuits, Shanghai Institute of Microsystem and Information Technology, Chinese Academy of Sciences, Shanghai, China. [5]School of Mechanics and Aerospace Engineering, State Key Laboratory of Structural Analysis, Optimization and CAE Software for Industrial Equipment, and International Research Center for Computational Mechanics, Dalian University of Technology, Dalian, China. [6]Department of Ophthalmology, Tongji Eye Institute, Tongji Hospital, School of Medicine, Tongji University, Shanghai, China. [7]State Key Laboratory of Integrated Chips and Systems, Fudan University, Shanghai, China. [8]Institute of Mechanics and Computational Engineering, Department of Aeronautics and Astronautics, College of Intelligent Robotics and Advanced Manufacturing, State Key Laboratory of Coatings for Advanced Equipment, Fudan University, Shanghai, China. [9]Neuromodulation and Brain-machine-interface Centre, MOE Frontiers Center for Brain Science, Fudan University, Shanghai, China. [10]These authors contributed equally: Lianjie Zhou, Pengchuan Liu.
✉e-mail: sem@fudan.edu.cn